Research Square

Preprints are preliminary reports that have not undergone peer review.
They should not be considered conclusive, used to inform clinical practice,
or referenced by the media as validated information.

Diurnal Land Surface Temperature Signals in Drought Propagation across Southeast Australia

Rui Fu

furui1118@gmail.com

Chiba University

Kazuhito Ichii

Chiba University

Yuhei Yamamoto

Chiba University

Beichen Zhang

Chiba University

Wei Li

Chiba University

Short Report

Keywords: Drought propagation, Diurnal temperature range, Himawari-8/9, Soil moisture, Vegetation greenness

Posted Date: November 24th, 2026

DOI: https://doi.org/10.21203/rs.3.rs-11649927/v1

License: This work is licensed under a Creative Commons Attribution 4.0 International License.
Read Full License

Additional Declarations: No competing interests reported.

Diurnal Land Surface Temperature Signals in Drought Propagation across Southeast Australia

Rui Fu[1,2*]

Correspondence: furui1118@gmail.com

Kazuhito Ichii[1,2*]

Correspondence: ichii@chiba-u.jp

Yuhei Yamamoto[1,2,3]

Beichen Zhang[1]

Wei Li[1]

1 Center for Environmental Remote Sensing (CEReS), Chiba University, 1-33, Yayoi-cho, Inage-ku, Chiba 263-8522, Japan

2 Graduate School of Science and Engineering, Chiba University, 1-33, Yayoi-cho, Inage-ku, Chiba 263-8522, Japan

3 Institute for Advanced Academic Research (IAAR), Chiba University, 1-33, Yayoi-cho, Inage-ku, Chiba 263-8522, Japan

Abstract

Drought propagation links precipitation deficits to changes in soil moisture, vegetation, and terrestrial water storage (TWS), but the timing and relative severity of thermal responses remain insufficiently quantified. We examined these responses across southeast Australia using the

Himawari-8/9 diurnal temperature range index (DTRI), precipitation anomaly (PA), surface soil moisture anomaly (SMA), normalized difference vegetation index (NDVI) anomaly, and TWS anomaly. Event-based analysis of the 2017–2019 Tinderbox drought quantified response delays and relative severity, expressed as response area ratios. DTRI responded after surface soil moisture drying and before vegetation greenness decline, with response delays of 4, 15, and 42 days for SMA, DTRI, and NDVI anomaly, respectively. The DTRI response was also weaker than the SMA response but stronger than the NDVI anomaly response in terms of relative severity. This ordering persisted across six climate zones wherever NDVI anomaly crossed the drought threshold. Soil moisture and NDVI responses were generally weaker in wetter zones. These findings place diurnal thermal responses between soil moisture depletion and greenness decline within drought propagation and support their complementary role in characterizing drought development.

Keywords

Drought propagation, Diurnal temperature range, Himawari-8/9, Soil moisture, Vegetation greenness

1 Introduction

Drought often begins with persistent precipitation deficits and can subsequently involve soil moisture depletion, vegetation stress, and reductions in terrestrial water storage (TWS) (Van Loon and Laaha, 2015; Wilhite and Glantz, 1985). This progression is commonly described as drought propagation, although its timing and strength differ among components of the land surface system (Entekhabi, 2023; Zhang et al., 2022). Previous studies have examined drought propagation through relationships among meteorological, soil moisture, vegetation, and hydrological indices (Apurv et al., 2017; Entekhabi, 2023; Vicente-Serrano et al., 2013). Thermal indices derived from land surface temperature (LST) can provide complementary information on land surface responses to water limitation (Yamamoto et al., 2023). Understanding the role of thermal responses within drought propagation is therefore important for interpreting drought development and assessing their potential value for drought monitoring.

LST provides information on surface water limitation because soil moisture influences evaporative cooling and surface heat storage (Anderson et al., 2013; McVicar and Jupp, 1998). Soil drying can reduce evapotranspiration and increase daytime surface temperatures, while moisture-dependent changes in thermal inertia can modify the diurnal temperature range (DTR) (Aït-Mesbah et al., 2015; Cheruy et al., 2017). Geostationary satellites resolve these variations through frequent observations, overcoming the limited diurnal sampling of polar-orbiting sensors (Yamamoto and Ishikawa, 2018). This high temporal resolution enables the derivation of thermal metrics based on morning warming, daytime temperature, and DTR, which have been used to monitor drought and vegetation drying (Hu et al., 2020; Yamamoto et al., 2023).

Yamamoto et al. (2023) found that DTR was more closely associated with surface soil moisture, whereas maximum LST showed stronger relationships with vegetation indices and latent heat flux, suggesting the potential of DTR-based indices for examining moisture-related

thermal responses. Cai et al. (2025) further evaluated correlations between surface–air temperature difference anomaly (SATDA), derived from Himawari-8 LST and gridded air temperature, and subsequent normalized difference vegetation index (NDVI) anomalies at different lead times, demonstrating the potential of SATDA for early detection of vegetation greenness decline. Although such lagged correlations reveal temporal relationships, they do not directly isolate individual drought events or quantify the attenuation of drought responses. Event-based analyses have quantified response delays and relative severity among conventional drought indicators (Entekhabi, 2023), providing a framework for comparing different stages of drought propagation. The relative timing and severity of LST-derived thermal responses within drought propagation remain insufficiently quantified, particularly across climate zones.

Southeast Australia spans contrasting climate zones and experienced the 2017–2019 Tinderbox drought (Devanand et al., 2024), providing a suitable setting for examining drought propagation. This study aims to clarify the role of diurnal thermal responses within drought propagation. To this end, we use the Himawari-8/9-derived diurnal temperature range index (DTRI), together with precipitation anomaly (PA), soil moisture anomaly (SMA), NDVI anomaly, and TWS anomaly across southeast Australia. Specifically, we (i) characterize the spatiotemporal evolution and lagged relationships of SMA, DTRI, NDVI anomaly, and TWS anomaly with PA; (ii) quantify their response delays and relative severity during meteorological drought events; and (iii) examine how these responses vary across climate zones.

2 Methods

2.1 Data sources and drought index construction

We analysed southeast Australia (138–154°E, 22–40°S) during 2016–2023, including the 2017–2019 Tinderbox drought (Devanand et al., 2024). The region spans arid inland landscapes

and humid coastal areas (Fig. S1). Table 1 summarizes the datasets used in this study. To remove seasonal variation, standardized anomalies were calculated as:

$$Z(t) = \frac{X_v(t) - \mu_d}{\sigma_d} \quad (1)$$

where $X_v(t)$ is the 30-day accumulated precipitation or 30-day mean of variable v, calculated using valid observations (Anderson et al., 2011; Cai et al., 2025). For each variable, μ_d and σ_d are the climatological mean and standard deviation for day of year *d*, estimated using a 10-day moving window over 2016–2023.

Daily precipitation was obtained from the Australian Water Availability Project (AWAP) at 0.05° resolution (Jones et al., 2009). Precipitation was accumulated over backward-looking 30-day windows, and the resulting totals were standardized using Eq. (1) to derive PA.

Surface soil moisture (0–5 cm) was obtained from the Soil Moisture Active Passive (SMAP) Enhanced L3 product (SPL3SMP_E, Version 5) on a 9-km grid (O'Neill et al., 2021). Available daily observations were averaged over backward-looking 30-day windows and standardized using Eq. (1) to derive SMA.

Himawari-8/9 LST was provided by the Center for Environmental Remote Sensing (CEReS), Chiba University, at 0.02° resolution and 10-min intervals (Yamamoto et al., 2022; Yamamoto et al., 2018). Daily DTR was calculated as the difference between mean midday LST (12:00–14:00 local time) and mean LST during the hour before sunrise. This window was defined using a longitude-based integer-hour offset, $t_{\mathrm{local}} = t_{\mathrm{UTC}} + \mathrm{fix}(\lambda/15)$, where time is expressed in hours, λ is longitude in degrees east, and fix truncates toward zero. The midday and pre-sunrise means required more than three and at least two valid observations, respectively. Daily DTR was averaged over backward-looking 30-day windows and standardized using Eq. (1) to derive DTRI. We used −DTRI in the analyses so that lower values consistently indicated drier conditions across

105 indices.

106 Daily NDVI was calculated as the 90th percentile of valid diurnal NDVI values derived from
107 Advanced Himawari Imager (AHI) red and near-infrared surface reflectance (Li et al., 2025;
108 Zhang et al., 2025a). Daily values were averaged over backward-looking 30-day windows and
109 standardized using Eq. (1) to derive NDVI anomaly. NDVI analyses were restricted to pixels with
110 mean NDVI ≥ 0.25 over 2016–2023.

111 Monthly TWS was obtained from the 0.5° climSSA gap-filled dataset based on RL06 mascon
112 solutions from the Center for Space Research (CSR). The dataset incorporates observations from
113 the Gravity Recovery and Climate Experiment (GRACE) and Gravity Recovery and Climate
114 Experiment Follow-On (GRACE-FO) missions (Zhang, 2023; Zhang et al., 2025b). The available
115 record spans 2002–2022, with 2016–2022 used in this study. TWS anomalies were calculated by
116 removing a linear trend and annual and semiannual harmonics over 2002–2022 and dividing the
117 residuals by their standard deviation. Monthly anomaly values were repeated on the daily analysis
118 grid. The resulting daily TWS anomaly series was then shifted 15 days later to account for the
119 backward-looking 30-day windows used for PA, SMA, DTRI, and NDVI anomaly.

120 Climate wetness (W) was the ratio of mean annual AWAP precipitation to mean annual
121 potential evapotranspiration (PET) from version 7 of the Australian Water Resources Assessment
122 Landscape model (AWRA-L v7) during 1993–2022 (Frost and Shokri, 2021). Six climate zones
123 were defined based on Cai et al. (2025) and Sahin (2012): arid ($W < 0.2$), semi-arid ($0.2 \leq W <$
124 0.5), dry sub-humid ($0.5 \leq W < 0.65$), semi-humid ($0.65 \leq W < 0.8$), humid ($0.8 \leq W < 1$), and
125 very humid ($W \geq 1$).

126 PA, DTRI, and NDVI anomalies were aggregated to a common approximately 9-km grid by
127 spatial averaging, while TWS anomaly was resampled to the same grid using the nearest-neighbor
128 method. Pixels burned during the 2019–2020 wildfires, identified using MCD64A1, were
129 excluded from the analyses (Giglio et al., 2021). Details of the lagged correlation analysis are

provided in the Supplementary Material.

Table 1. Five drought indices, climate zones and fire mask.

Index or use	Source	Temporal resolution	Spatial resolution	Reference
PA	AWAP precipitation	Daily	0.05°	Jones et al. (2009)
SMA	SMAP soil moisture	Daily	9 km	O'Neill et al. (2021)
−DTRI	Himawari-8/9 AHI LST	10 min	0.02°	Yamamoto et al. (2018); Yamamoto et al. (2022)
NDVI anomaly	Himawari-8/9 AHI red and near-infrared land surface reflectance	10 min	0.01°	Li et al. (2025)
TWS anomaly	climSSA gap-filled GRACE/GRACE-FO TWS	Monthly	0.5°	Zhang (2023)
Climate zones	AWRA-L v7 PET; AWAP precipitation	Daily	0.05°	Frost and Shokri (2021)
Fire mask	MCD64A1 burned area	Monthly	500 m	Giglio et al. (2021)

2.2 Event-based drought propagation analysis

Event-based analysis, adapted from Entekhabi (2023), quantified response delay and relative severity during 2017–2019 for the study region and each climate zone. At each pixel, meteorological drought events were continuous periods with PA < −0.5 lasting at least 60 days. Responses were evaluated within these PA events. Each index was converted to pixel-specific percentile ranks (P) on a 0–1 scale using its available record. DTRI ranks were calculated from the original DTRI and reversed as one minus the original rank, so lower P indicated drier conditions for every index. Cumulative precipitation anomaly (C_{PA}) was the running sum of daily PA from each event onset.

Event-day observations were pooled into 100 C_{PA} intervals of width 1 between 0 and −100. For each interval, we calculated mean P and the median number of days since PA drought onset (T), counting onset as day 1. Intervals were examined from C_{PA} of 0 toward −100. Response delay was the corresponding T when mean P first fell below 0.3. Delay was undefined if no interval met this criterion within that range. Drought severity was calculated by summing the differences between 0.5 and mean P across C_{PA} intervals satisfying the drought threshold

147 ($\bar{P}$<0.3).

$$S_v = \sum_{J \in B_v} \left(0.5 - \overline{P_{v,J}}\right) \quad (2)$$

148 where $\overline{P_{v,J}}$ denotes mean P for response variable v within C_{PA} interval J, and B_v is the set of
149 intervals satisfying ($\overline{P_{v,J}}$<0.3). The same calculation was applied to PA to obtain S_{PA}. The
150 response area ratio was then defined as

$$R_v = S_v / S_{\mathrm{PA}} \quad (3)$$

151 The response area ratio quantifies relative severity in percentile space. R_v below 1 indicates a
152 weaker drought response than the PA reference, whereas R_v above 1 indicates a stronger
153 response. For the event-based analyses, the mean-NDVI mask was applied to all indices.

154 Uncertainty in response delay and response area ratio was estimated using 2,000 bootstrap
155 resamples of pixel-level PA drought events within each climate zone. Complete events were
156 sampled with replacement, preserving the original number of events, with identical event draws
157 used across all indices to maintain paired comparisons. For each resample, the pooled percentile-
158 response curves were reconstructed, and both response delay and response area ratio were
159 recalculated. Marginal 95% confidence intervals were obtained from the 2.5th and 97.5th
160 percentiles of the corresponding bootstrap distributions.

161 3 Results

162 3.1 Overall drought evolution and propagation overview

163 The regional time series revealed distinct temporal responses among the drought indices, with
164 −DTRI generally following SMA and preceding NDVI anomaly, while TWS anomaly exhibited
165 a more persistent response (Fig. 1). PA, SMA, and −DTRI exhibited more pronounced short-term
166 fluctuations, whereas NDVI and TWS anomalies showed smoother variations. During the 2017–

2019 drought, all five indices exhibited periods of negative anomalies, but their responses differed in timing and persistence. While PA and SMA showed intermittent recoveries, NDVI anomaly declined more gradually, and TWS anomaly remained negative through much of 2020–2021. During 2022, wetter conditions were accompanied by periods of positive anomalies across the available indices.

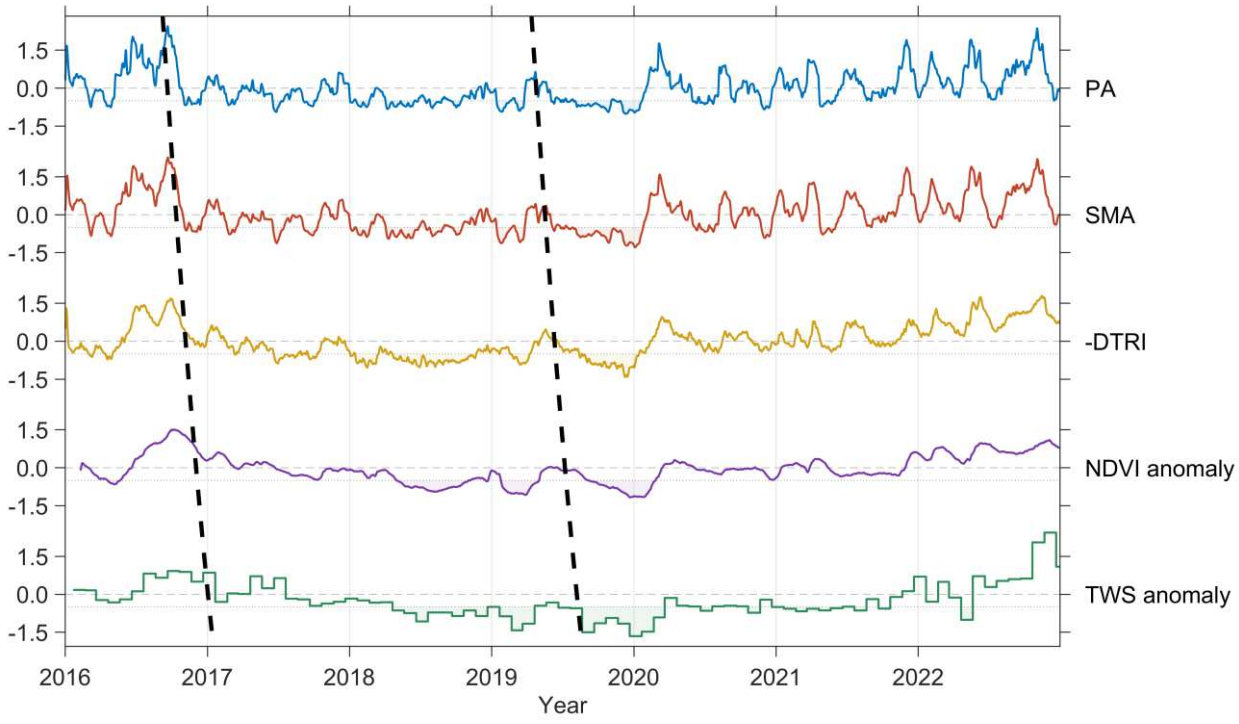

Fig. 1. Regional mean standardized anomalies across southeast Australia during 2016–2022. Rows show PA, SMA, −DTRI, NDVI anomaly, and TWS anomaly from top to bottom. Dashed and dotted horizontal lines mark 0 and −0.5, respectively. The slanted black dashed lines are provided as visual guides to illustrate the temporal sequence of responses among the indices.

178 The spatial evolution of drought-related anomalies during late 2016 further illustrated
179 differences in the timing and spatial extent of these responses (Fig. 2). Negative PA anomalies
180 first became apparent in the northeastern part of the study region around day 285 and subsequently
181 spread across much of the study region. SMA showed a similar but delayed spatial progression,
182 with negative anomalies becoming widespread by day 325. Negative −DTRI anomalies emerged
183 locally around day 305 and gradually expanded across parts of the region during subsequent
184 snapshots. In contrast, NDVI anomaly remained predominantly positive over much of the
185 vegetated area, with negative anomalies becoming more apparent in the northeast around day 345.
186 TWS anomaly declined more gradually but remained predominantly positive throughout the
187 displayed period. Complementary lagged correlation analyses showed median maximum
188 correlations with PA of 0.82 for SMA, 0.63 for −DTRI, 0.53 for NDVI anomaly, and 0.41 for
189 TWS anomaly (Fig. S2). The corresponding median lags were 1, 10, 30, and 30 days, respectively
190 (Fig. S3).

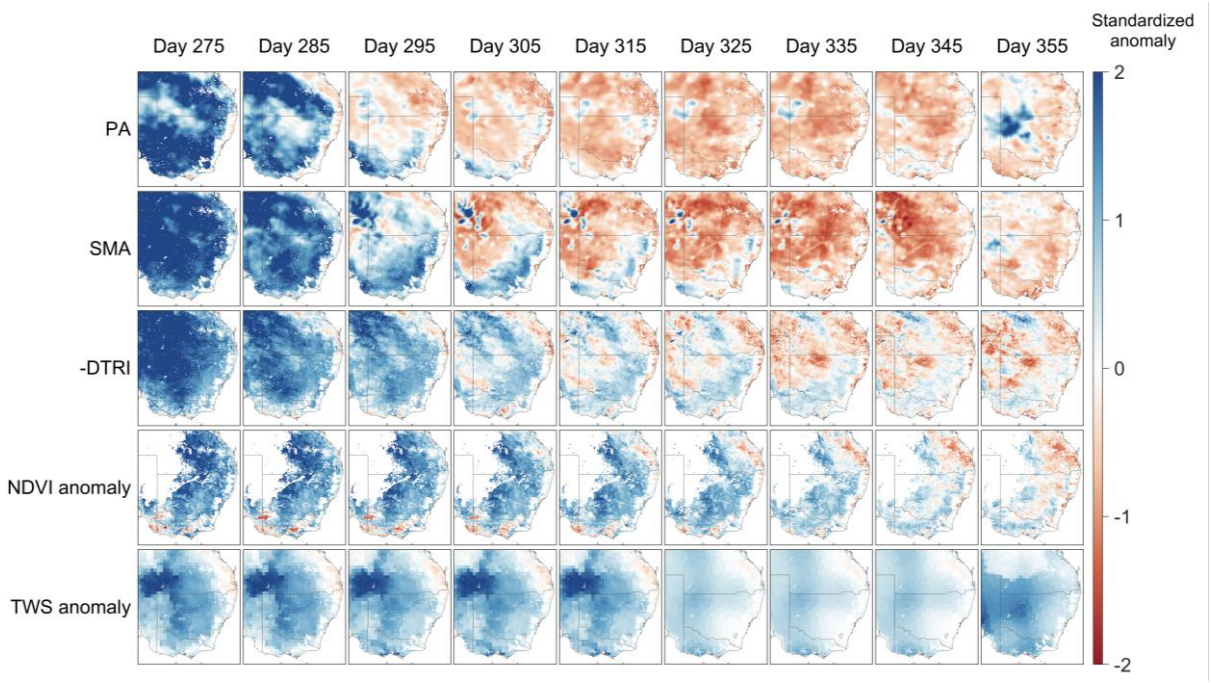

Fig. 2. Spatial evolution of standardized anomalies at 10-day intervals during late 2016. Rows show PA, SMA, −DTRI, NDVI anomaly, and TWS anomaly. Blue and red indicate positive and negative anomalies, respectively; sign reversal of DTRI makes negative anomalies indicate drier conditions. NDVI anomaly includes only pixels with mean NDVI ≥ 0.25.

3.2 Event-based propagation: response delay and relative severity

Event-based analysis revealed that the −DTRI response to meteorological drought was intermediate between SMA and NDVI anomaly in both response delay and relative severity (Fig. 3). For all eligible pixels pooled together, SMA reached the drought percentile threshold first, with a response delay of 4 days, followed by −DTRI (15 days), NDVI anomaly (42 days), and TWS anomaly (49 days). The corresponding response area ratios were 1.06, 0.88, 0.57, and 0.46, respectively, indicating that the thermal response was weaker than the soil moisture response but stronger than the vegetation greenness response.

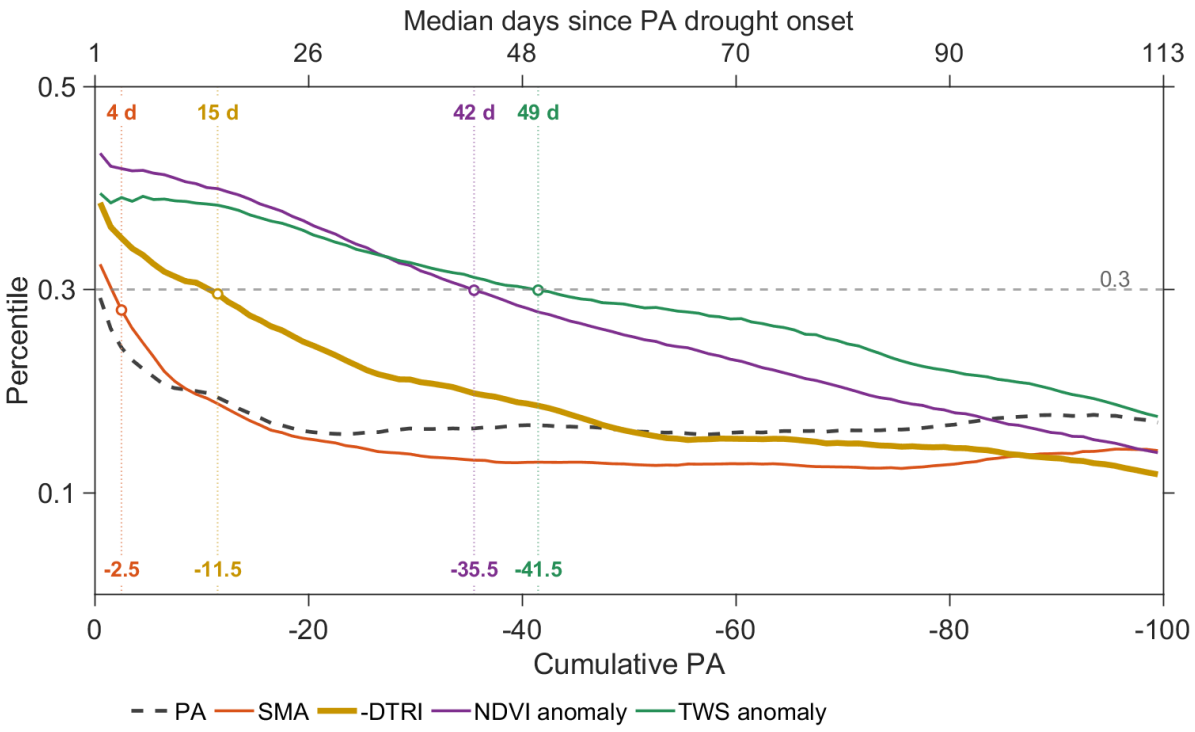

Fig. 3. Mean percentile responses of PA, SMA, −DTRI, NDVI anomaly, and TWS anomaly during the 2017–2019 meteorological drought events (PA < −0.5 for ≥60 days). Event-day observations are grouped into unit-width cumulative PA intervals, with the upper axis indicating the corresponding median days since PA drought onset. The horizontal dashed line marks the percentile-rank threshold of 0.3, while the vertical dotted lines indicate when each index first crosses this threshold, with the corresponding cumulative PA and elapsed days annotated. Lower percentiles indicate drier conditions. All indices are masked using unburned pixels with mean NDVI ≥ 0.25.

Across climate zones, −DTRI consistently occupied an intermediate position between SMA and NDVI anomaly in both response delay and relative severity (Fig. 4). SMA delays ranged from 2 to 16 days, compared with 11 to 41 days for −DTRI. SMA response area ratios declined from approximately 1 in the drier zones to 0.68 in the very humid zone. NDVI anomaly responses were more attenuated toward wetter zones, with particularly small response area ratios in the semi-humid and humid zones. In the very humid zone, NDVI anomaly did not cross the threshold, so its response delay was undefined. TWS anomaly responded earlier than NDVI anomaly in the dry sub-humid, semi-humid, and humid zones, although it responded later in the arid and semi-arid zones. Overall, response delays tended to be shorter in drier zones and longer in wetter zones, although this trend was not monotonic.

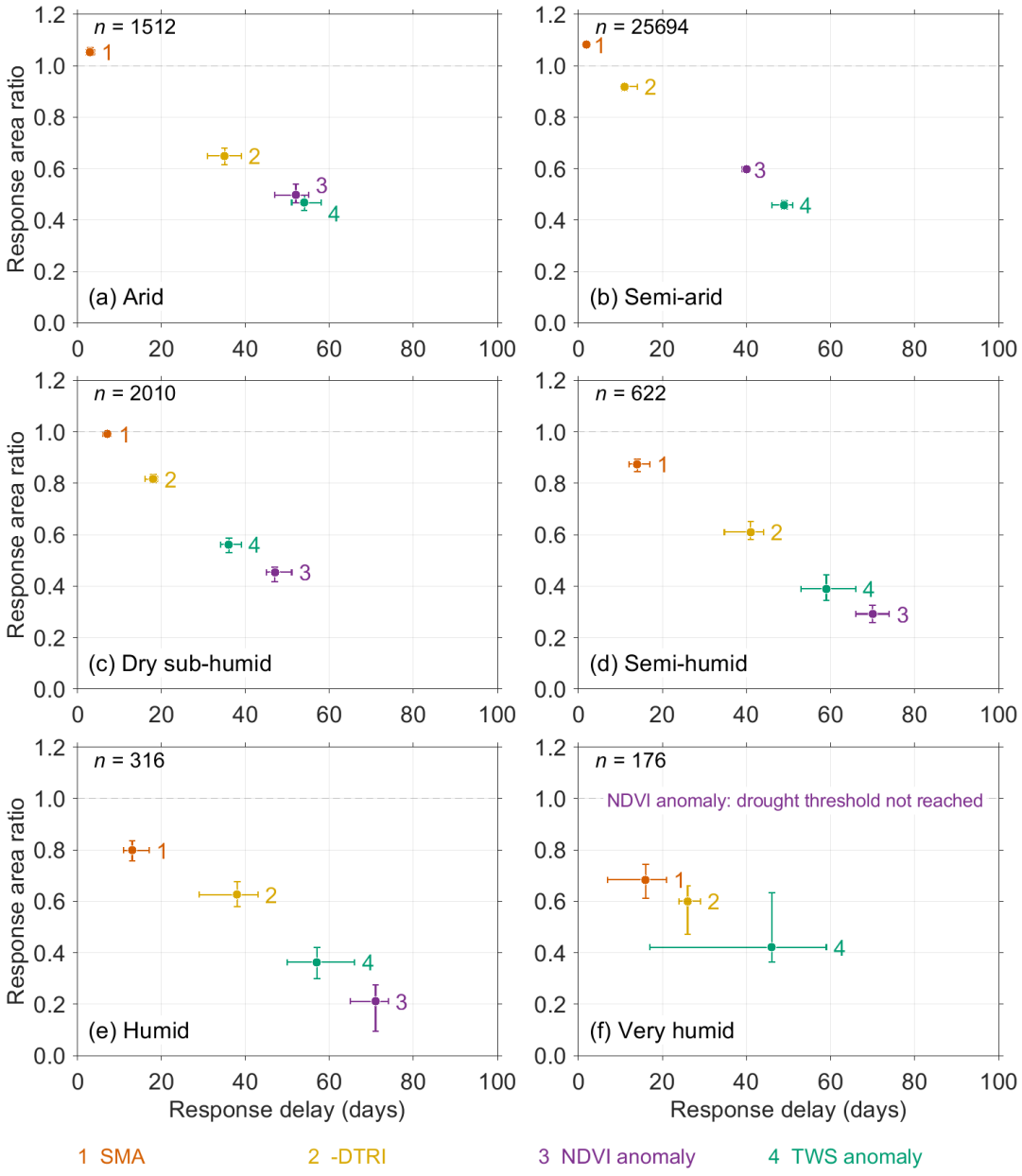
n = 1512
(a) Arid
n = 25694
(b) Semi-arid
n = 2010
(c) Dry sub-humid
n = 622
(d) Semi-humid
n = 316
(e) Humid
n = 176
NDVI anomaly: drought threshold not reached
(f) Very humid
Response area ratio
Response delay (days)
1 SMA
2 -DTRI
3 NDVI anomaly
4 TWS anomaly

224

Fig. 4. Response delay and response area ratio by climate zone during 2017–2019. Labels 1–4 denote SMA, −DTRI, NDVI anomaly, and TWS anomaly; *n* denotes the number of pixel-level PA events. Response delay is the pooled event-based estimate defined in Section 2.2; response area ratio is the ratio of target severity to PA severity. Horizontal and vertical error bars indicate marginal 95% bootstrap confidence intervals for response delay and response area ratio, respectively, based on 2,000 paired resamples of complete PA drought events within each climate zone.

4 Discussion

DTRI occupied an intermediate position between surface soil moisture and vegetation greenness in both response timing and relative severity (Fig. 3). Agreement between the lagged correlation and event-based analyses supports the intermediate timing of DTRI between SMA and NDVI anomaly (Fig. 3 and Fig. S3). These results extend observational assessments of drought propagation across water storage and vegetation indices by incorporating a diurnal thermal response (Entekhabi, 2023; Zhang et al., 2022).

The relatively rapid SMA response reflects reduced rainfall replenishment combined with continued evaporative losses from the shallow soil layer (Apurv et al., 2017). Soil drying can restrict evapotranspiration and evaporative cooling, increasing daytime surface warming; moisture-dependent changes in soil heat storage can also alter the diurnal temperature range (Anderson et al., 2011; Yamamoto et al., 2023). Thermal observations responded before NDVI showed a sustained decline (Fig. 3 and Fig. 4), consistent with the potential for earlier thermal detection of vegetation drying reported by Yamamoto et al. (2023) and Cai et al. (2025). Vegetation greenness can remain comparatively stable during initial surface drying, producing a

247 later NDVI response even when water limitation has begun (Vicente-Serrano et al., 2013). NDVI
248 persistence describes a delayed greenness response; it does not establish when physiological water
249 stress began. TWS integrates changes in several water stores and therefore represents a broader
250 storage response than surface soil moisture (Entekhabi, 2023). Its smoother regional evolution
251 and later event-based threshold crossing are consistent with this integration (Fig. 1 and Fig. 3).

252 The observed differences in drought propagation across climate zones may reflect variations
253 in water storage and the balance between precipitation supply and evaporative demand (Apurv et
254 al., 2017; Tijdeman et al., 2018). In humid regions, soil water storage and subsurface water
255 contributions can buffer short-term precipitation deficits, attenuating drought responses. In arid
256 and semi-arid regions, limited available water can be depleted rapidly through evaporative losses
257 when rainfall replenishment declines, allowing precipitation deficits to be reflected more directly
258 in land surface conditions. These buffering mechanisms may help explain the more attenuated
259 responses toward wetter climate zones. Where NDVI crossed the drought threshold, DTRI
260 consistently responded after SMA and before NDVI (Fig. 4). These differences suggest that
261 climate-dependent water availability and storage may influence drought propagation, although
262 local conditions can modify the response timing.

263 These findings highlight the potential value of thermal observations for drought monitoring
264 and early warning. A local example further illustrates the spatial detail provided by DTRI, with
265 the 2-km observations revealing sub-grid variability that is smoothed at 9 km (Fig. S4). The
266 corresponding time series also show a thermal response preceding the decline in NDVI anomaly.
267 By positioning DTRI within the drought propagation pathway, this study shows that thermal
268 signals can provide information on drought development before vegetation greenness declines.
269 Combining thermal, soil moisture, and vegetation observations may therefore improve the
270 detection and characterization of emerging drought conditions. Radiation and atmospheric
271 conditions can also influence DTR (Cheruy et al., 2017), while clear-sky sampling, 30-day

aggregation, and the monthly resolution of TWS may affect the estimated response timing. Further evaluation across other regions and drought events would help establish the broader applicability of these findings.

5 Conclusion

This study incorporated Himawari-8/9-derived DTRI into an observational analysis of drought propagation across southeast Australia. An event-based approach compared responses at common levels of cumulative PA during the 2017–2019 Tinderbox drought, quantifying response delays and relative severity for surface soil moisture, diurnal thermal conditions, vegetation greenness, and TWS. SMA responded rapidly to meteorological drought, with a response delay of 4 days and a response area ratio close to unity (1.06). DTRI responded after 15 days with a ratio of 0.88, placing it between SMA and NDVI anomaly in both timing and relative severity. NDVI anomaly and TWS anomaly responded later, after 42 and 49 days, with smaller ratios of 0.57 and 0.46, respectively. Complementary lagged correlations supported the intermediate timing of DTRI.

Across climate zones, DTRI responded after SMA and before NDVI anomaly wherever NDVI anomaly crossed the drought threshold. SMA and NDVI anomaly responses were generally weaker in wetter zones, while response delays tended to be shorter in drier zones. These results show that diurnal thermal observations capture a stage of drought development between surface soil moisture drying and vegetation greenness decline. Their inclusion can complement soil moisture and vegetation indices in characterizing drought propagation. Further application of this framework to other geostationary satellite observation domains and a wider range of drought events is needed to assess its broader applicability.

Acknowledgements

This work was supported by JSPS KAKENHI (JP22H05004), Core-to-Core Program (JPJSCCA20220008), the IAAR Research Support Program of Chiba University and Virtual Laboratory (VL) Program by MEXT, Japan and JST SPRING (Grant Number JPMJSP2109).

Statements and Declarations

Competing interests

The authors declare that they have no relevant financial or non-financial interests to disclose.

Data Availability

The AWAP precipitation data were obtained from the Australian Bureau of Meteorology (https://www.bom.gov.au/climate/maps/rainfall/), and the AWRA-L v7 potential evapotranspiration data were obtained from the Australian Water Outlook (https://awo.bom.gov.au/). SMAP soil moisture data (SPL3SMP_E, Version 5) are available from the NASA National Snow and Ice Data Center (https://doi.org/10.5067/4DQ54OUIJ9DL). The climSSA gap-filled GRACE/GRACE-FO terrestrial water storage data are available from Figshare (https://doi.org/10.6084/m9.figshare.24773232), and the MCD64A1 burned-area data are available from NASA LP DAAC (https://doi.org/10.5067/MODIS/MCD64A1.061). Himawari-8/9 land surface temperature and surface reflectance products were provided by the Center for Environmental Remote Sensing (CEReS), Chiba University. The processed data supporting the findings of this study are available from the corresponding author upon reasonable request, subject to applicable data-use conditions.

References

Aït-Mesbah, S., Dufresne, J. L., Cheruy, F. & Hourdin, F. 2015. The role of thermal inertia in the representation of mean and diurnal range of surface temperature in semiarid and arid regions. *Geophysical Research Letters,* 42**,** 7572-7580. https://doi.org/10.1002/2015GL065553.

Anderson, M. C., Hain, C., Otkin, J., Zhan, X., Mo, K., Svoboda, M., Wardlow, B. & Pimstein, A. 2013. An intercomparison of drought indicators based on thermal remote sensing and NLDAS-2 simulations with U.S. Drought Monitor classifications. *Journal of Hydrometeorology,* 14**,** 1035-1056. https://doi.org/10.1175/JHM-D-12-0140.1.

Anderson, M. C., Hain, C., Wardlow, B., Pimstein, A., Mecikalski, J. R. & Kustas, W. P. 2011. Evaluation of Drought Indices Based on Thermal Remote Sensing of Evapotranspiration over the Continental United States. *Journal of Climate,* 24**,** 2025-2044. https://doi.org/10.1175/2010jcli3812.1.

Apurv, T., Sivapalan, M. & Cai, X. 2017. Understanding the Role of Climate Characteristics in Drought Propagation. *Water Resources Research,* 53**,** 9304-9329. https://doi.org/10.1002/2017wr021445.

Cai, D., McVicar, T. R., Van Niel, T. G., Donohue, R. J., Yamamoto, Y., Stewart, S. B., Ichii, K. & Stenson, M. P. 2025. Using sub-diurnal surface-air temperature difference anomaly derived from Himawari-8 geostationary satellite and meteorological grids for early detection of vegetation drought stress: Application to Australia's 2017–2019 Tinderbox Drought.

Remote Sensing of Environment, 327**,** 114768. https://doi.org/10.1016/j.rse.2025.114768.

Cheruy, F., Dufresne, J. L., Aït Mesbah, S., Grandpeix, J. Y. & Wang, F. 2017. Role of soil thermal inertia in surface temperature and soil moisture-temperature feedback. *Journal of Advances in Modeling Earth Systems,* 9**,** 2906-2919. https://doi.org/10.1002/2017MS001036.

Devanand, A., Falster, G. M., Gillett, Z. E., Hobeichi, S., Holgate, C. M., Jin, C., Mu, M., Parker, T., Rifai, S. W., Rome, K. S., Stojanovic, M., Vogel, E., Abram, N. J., Abramowitz, G., Coats, S., Evans, J. P., Gallant, A. J. E., Pitman, A. J., Power, S. B., Rauniyar, S. P., Taschetto, A. S. & Ukkola, A. M. 2024. Australia's Tinderbox Drought: An extreme natural event likely worsened by human-caused climate change. *Science Advances,* 10**,** eadj3460. https://doi.org/10.1126/sciadv.adj3460.

Entekhabi, D. 2023. Propagation in the Drought Cascade: Observational Analysis Over the Continental US. *Water Resources Research,* 59**,** e2022WR032608. https://doi.org/10.1029/2022wr032608.

Frost, A. J. & Shokri, A. 2021. The Australian Landscape Water Balance model (AWRA-L v7): Technical Description of the Australian Water Resources Assessment Landscape model version 7. 1.0.6 ed. Melbourne, Australia: Bureau of Meteorology.

Giglio, L., Justice, C., Boschetti, L. & Roy, D. 2021. MODIS/Terra+Aqua Burned Area Monthly L3 Global 500m SIN Grid V061. NASA Land Processes Distributed Active Archive Center. https://doi.org/10.5067/MODIS/MCD64A1.061.

354 Hu, T., Renzullo, L. J., van Dijk, A. I. J. M., He, J., Tian, S., Xu, Z., Zhou, J., Liu, T. & Liu, Q.
355 2020. Monitoring agricultural drought in Australia using MTSAT-2 land surface temperature
356 retrievals. *Remote Sensing of Environment,* 236**,** 111419.
357 https://doi.org/10.1016/j.rse.2019.111419.
358 Jones, D. A., Wang, W. & Fawcett, R. 2009. High-quality spatial climate data-sets for Australia.
359 *Australian Meteorological and Oceanographic Journal,* 58**,** 233-248.
360 https://doi.org/10.1071/ES09032.
361 Li, W., Ichii, K., Zhang, B., Yamamoto, Y., Yang, W., Miura, T., Yoshioka, H., Matsuoka, M.,
362 Obata, K., Sharma, R. C., Yamamoto, H., Irie, H., Khatri, P., Liley, B., Morino, I., Takenaka,
363 H. & Higuchi, A. 2025. Estimation and Evaluation of Land Surface Reflectance from a Next-
364 Generation Geostationary Meteorological Satellite, Himawari-8/9 AHI. *Journal of the*
365 *Meteorological Society of Japan. Ser. II,* 103**,** 87-109. https://doi.org/10.2151/jmsj.2025-005.
366 McVicar, T. R. & Jupp, D. L. B. 1998. The current and potential operational uses of remote sensing
367 to aid decisions on drought exceptional circumstances in Australia: a review. *Agricultural*
368 *Systems,* 57**,** 399-468. https://doi.org/10.1016/S0308-521X(98)00026-2.
369 O'Neill, P. E., Chan, S., Njoku, E. G., Jackson, T., Bindlish, R., Chaubell, J. & Colliander, A. 2021.
370 SMAP Enhanced L3 Radiometer Global and Polar Grid Daily 9 km EASE-Grid Soil
371 Moisture, Version 5. NASA National Snow and Ice Data Center Distributed Active Archive
372 Center. https://doi.org/10.5067/4DQ54OUIJ9DL.

373 Sahin, S. 2012. An aridity index defined by precipitation and specific humidity. *Journal of*
374 *Hydrology,* 444-445**,** 199-208. https://doi.org/10.1016/j.jhydrol.2012.04.019.
375 Tijdeman, E., Barker, L. J., Svoboda, M. D. & Stahl, K. 2018. Natural and Human Influences on
376 the Link Between Meteorological and Hydrological Drought Indices for a Large Set of
377 Catchments in the Contiguous United States. *Water Resources Research,* 54**,** 6005-6023.
378 https://doi.org/10.1029/2017wr022412.
379 Van Loon, A. F. & Laaha, G. 2015. Hydrological drought severity explained by climate and
380 catchment characteristics. *Journal of Hydrology,* 526**,** 3-14.
381 https://doi.org/10.1016/j.jhydrol.2014.10.059.
382 Vicente-Serrano, S. M., Gouveia, C., Camarero, J. J., Beguería, S., Trigo, R., López-Moreno, J. I.,
383 Azorín-Molina, C., Pasho, E., Lorenzo-Lacruz, J., Revuelto, J., Morán-Tejeda, E. &
384 Sanchez-Lorenzo, A. 2013. Response of vegetation to drought time-scales across global land
385 biomes. *Proceedings of the National Academy of Sciences,* 110**,** 52-57.
386 https://doi.org/10.1073/pnas.1207068110.
387 Wilhite, D. A. & Glantz, M. H. 1985. Understanding: the Drought Phenomenon: The Role of
388 Definitions. *Water International,* 10**,** 111-120. https://doi.org/10.1080/02508068508686328.
389 Yamamoto, Y., Ichii, K., Ryu, Y., Kang, M. & Murayama, S. 2022. Uncertainty quantification in
390 land surface temperature retrieved from Himawari-8/AHI data by operational algorithms.
391 *ISPRS Journal of Photogrammetry and Remote Sensing,* 191**,** 171-187.

https://doi.org/10.1016/j.isprsjprs.2022.07.008.

Yamamoto, Y., Ichii, K., Ryu, Y., Kang, M., Murayama, S., Kim, S.-J. & Cleverly, J. R. 2023. Detection of vegetation drying signals using diurnal variation of land surface temperature: Application to the 2018 East Asia heatwave. *Remote Sensing of Environment,* 291**,** 113572. https://doi.org/10.1016/j.rse.2023.113572.

Yamamoto, Y. & Ishikawa, H. 2018. Thermal land surface emissivity for retrieving land surface temperature from Himawari-8. *Journal of the Meteorological Society of Japan. Ser. II,* 96B**,** 43-58. https://doi.org/10.2151/jmsj.2018-004.

Yamamoto, Y., Ishikawa, H., Oku, Y. & Hu, Z. 2018. An Algorithm for Land Surface Temperature Retrieval Using Three Thermal Infrared Bands of Himawari-8. *Journal of the Meteorological Society of Japan. Ser. II,* 96B**,** 59-76. https://doi.org/10.2151/jmsj.2018-005.

Zhang, B., Ichii, K., Li, W., Yamamoto, Y., Yang, W., Sharma, R. C., Yoshioka, H., Obata, K., Matsuoka, M. & Miura, T. 2025a. Evaluation of Himawari-8/AHI land surface reflectance at mid-latitudes using LEO sensors with off-nadir observation. *Remote Sensing of Environment,* 316**,** 114491. https://doi.org/10.1016/j.rse.2024.114491.

Zhang, X. 2023. Monthly SSA-gapfilled and climSSA-gapfilled data based on CSR GRACE and GRACE-FO RL06 Mascons since 2002. figshare. https://doi.org/10.6084/m9.figshare.24773232.

Zhang, X., Hao, Z., Singh, V. P., Zhang, Y., Feng, S., Xu, Y. & Hao, F. 2022. Drought propagation

under global warming: Characteristics, approaches, processes, and controlling factors. *Science of The Total Environment,* 838**,** 156021. https://doi.org/10.1016/j.scitotenv.2022.156021.

Zhang, X., Ren, C., Wang, Z., Li, X. & Zhang, Y. 2025b. Gap-filling GRACE and GRACE-FO data with a climate adjustment scheme using Singular Spectrum analysis. *Journal of Hydrology,* 653**,** 132782. https://doi.org/10.1016/j.jhydrol.2025.132782.

Supplementary Files

This is a list of supplementary files associated with this preprint. Click to download.

- Supplementary.docx